


## Article

# Sodium Pre-Intercalation-Based $\text{Na}_3\text{-}\delta\text{-MnO}_2\text{@CC}$ for High-Performance Aqueous Asymmetric Supercapacitor: Joint Experimental and DFT Study

Anis Ur Rahman<sup>1</sup>, Nighat Zarshad<sup>2</sup>, Wu Jianguhua<sup>3</sup>, Muslim Shah<sup>4</sup>, Sana Ullah<sup>4</sup>, Guigen Li<sup>1,5,\*</sup>, Muhammad Tariq<sup>6</sup>  and Asad Ali<sup>4,\*</sup>

- <sup>1</sup> Institute of Chemistry and BioMedical Sciences, School of Chemistry and Chemical Engineering, Nanjing University, Nanjing 210023, China
- <sup>2</sup> Department of Polymer Science, School of Chemistry and Chemical Engineering, Southeast University, Nanjing 211189, China
- <sup>3</sup> National Laboratory of Solid State Microstructures, Collaborative Innovation Center of Advanced Microstructures, College of Engineering and Applied Sciences, Nanjing University, Nanjing 210093, China
- <sup>4</sup> Department of Chemistry, Faculty of Chemical and Life Sciences, Abdul Wali Khan University, Mardan 23200, Pakistan
- <sup>5</sup> Department of Chemistry and Biochemistry, Texas Tech University, Lubbock, TX 79409, USA
- <sup>6</sup> Department of PCB, Bayazid Rokhan Institute of Higher Studies, Kabul 1002, Afghanistan
- \* Correspondence: guigen.li@ttu.edu (G.L.); asadali@awkum.edu.pk (A.A.)



**Citation:** Rahman, A.U.; Zarshad, N.; Jianguhua, W.; Shah, M.; Ullah, S.; Li, G.; Tariq, M.; Ali, A. Sodium Pre-Intercalation-Based  $\text{Na}_3\text{-}\delta\text{-MnO}_2\text{@CC}$  for High-Performance Aqueous Asymmetric Supercapacitor: Joint Experimental and DFT Study. *Nanomaterials* **2022**, *12*, 2856. <https://doi.org/10.3390/nano12162856>

Academic Editors: Jin An Wang, Lifang Chen and Luis Enrique Noreña

Received: 13 May 2022

Accepted: 25 July 2022

Published: 18 August 2022

**Publisher's Note:** MDPI stays neutral with regard to jurisdictional claims in published maps and institutional affiliations.



**Copyright:** © 2022 by the authors. Licensee MDPI, Basel, Switzerland. This article is an open access article distributed under the terms and conditions of the Creative Commons Attribution (CC BY) license (<https://creativecommons.org/licenses/by/4.0/>).

**Abstract:** Electrochemical energy storage devices are ubiquitous for personal electronics, electric vehicles, smart grids, and future clean energy demand. SCs are EES devices with excellent power density and superior cycling ability. Herein, we focused on the fabrication and DFT calculations of  $\text{Na}_3\text{-}\delta\text{-MnO}_2$  nanocomposite, which has layered  $\text{MnO}_2$  redox-active sites, supported on carbon cloth.  $\text{MnO}_2$  has two-dimensional diffusion channels and is not labile to structural changes during intercalation; therefore, it is considered the best substrate for intercalation. Cation pre-intercalation has proven to be an effective way of increasing inter-layered spacing, optimizing the crystal structure, and improving the relevant electrochemical behavior of asymmetric aqueous supercapacitors. We successfully established  $\text{Na}^+$  pre-intercalated  $\delta\text{-MnO}_2$  nanosheets on carbon cloth via one-pot hydrothermal synthesis. As a cathode, our prepared material exhibited an extended potential window of 0–1.4 V with a remarkable specific capacitance of  $546 \text{ F g}^{-1}$  ( $300 \text{ F g}^{-1}$  at  $50 \text{ A g}^{-1}$ ). Moreover, when this cathode was accompanied by an N-AC anode in an asymmetric aqueous supercapacitor, it illustrated exceptional performance ( $64 \text{ Wh kg}^{-1}$  at a power density of  $1225 \text{ W kg}^{-1}$ ) and incomparable potential window of 2.4 V and 83% capacitance retention over 10,000 cycles with a great Columbic efficiency.

**Keywords:** manganese oxide; pre-intercalation; specific capacitance; wide potential window; asymmetric aqueous supercapacitor; DFT calculation

## 1. Introduction

The continuous depletion of non-renewable energy resources as a consequence of rapid economic development around the globe has forced researchers to seek technological evolution for the future to satisfy the demands of efficient and renewable energy. In this regard, the supercapacitor stands out as the most promising candidate owing to its fast charge/discharge rate, supreme cyclic stability [1], as well as high power density [2]. However, the lower energy density of the currently employed supercapacitors is a limiting factor for their practical applicability [3]. Therefore, it is indispensable to boost the energy density of supercapacitors without impacting their stability and power density. This can be accomplished by either enhancing the specific capacitance or cell voltage. The construction of an asymmetric supercapacitor is a viable route for achieving high cell

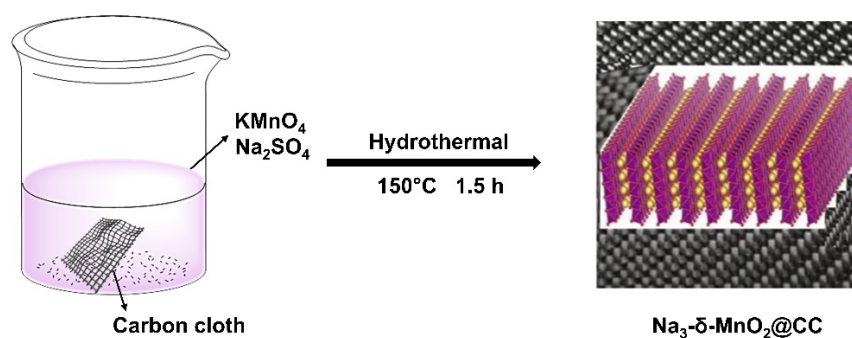
voltage, where the negative electrode is present at a lower potential, while the positive electrode is present at a higher potential and operates in a different potential window [4,5]. This results in improved cell voltage and energy density of the material. However, the maximum cell voltage obtained so far lies between 1.4 and 2.0 V, which is still not enough to practically fulfill the energy demands [6,7]. Therefore, the quest of developing asymmetric supercapacitors with a voltage range higher than 2.0 V is still an untangled issue [8].

As a cathode material, MnO<sub>2</sub> has been a fascinating choice because of its large theoretical specific capacitance value ( $\sim 1370 \text{ F g}^{-1}$ ) and wide potential window ( $\sim 1.0 \text{ V}$ ) [9–12]. MnO<sub>2</sub> can be found in a variety of crystal structures, such as  $\alpha$ ,  $\beta$ ,  $\gamma$ ,  $\delta$ , and  $\lambda$  MnO<sub>2</sub>. The electrochemical properties of  $\alpha$ ,  $\beta$ , and  $\gamma$ -MnO<sub>2</sub> are associated with their chain/tunnel type crystal structure facilitating electron transport for achieving high specific capacitance [13]. Moreover, the layered sheet-like structure of  $\delta$ -MnO<sub>2</sub> makes it suitable for the intercalation of various cations, so as to increase the interlayer spacing, improving the migration rate of electrons, which increases the specific capacitance [14,15].

Pre-intercalation of MnO<sub>2</sub> has acquired much attention in recent years as a viable strategy to escalate the electrochemical efficiency of MnO<sub>2</sub>-based supercapacitors [16]. Pre-intercalated MnO<sub>2</sub> has several ions intercalated into the redox channel and the interlayer of MnO<sub>2</sub> before electrochemical measurements [17]. Chemical bonding allows these intercalated ions to interact with the host framework and the incorporated carrier ions on an electrostatic and physical level, which has a significant impact on the intrinsic structure of MnO<sub>2</sub> and the carrier ion transport kinetics [18,19]. High specific surface area and optimized channels available for quick and reversible ion injection and extraction play a key role in achieving excellent specific capacitance, increased energy density, and extended potential window [20].

To elucidate the availing influence of pre-intercalation, some published works are mentioned below. It has been proposed [21] that pre-intercalated K<sup>+</sup> ions inside  $2 \times 2$  tunnels of MnO<sub>2</sub> would improve Li<sup>+</sup> diffusivity by increasing electronic conductivity and interlayer spacing and electrostatic interactions between the inserted Li<sup>+</sup> ions and host anions. On the other hand, they are thought to have a big impact on the activation barrier for Li<sup>+</sup> hopping in the layered lithium transition metal oxides [22–24]. The charge shielding property of crystal water lowers electrostatic interactions between the carrier ions and host anions, improving carrier ion diffusion kinetics in MnO<sub>2</sub> cathodes, according to the literature [25,26].

We intended to construct ultra-thin Na<sup>+</sup> ions pre-intercalated MnO<sub>2</sub> cathode material on carbon cloth (CC), as shown in Scheme 1, a high-performance supercapacitor with an extended working potential window of 0–1.4 V, which has a very high reversible capacitance of  $560 \text{ F g}^{-1}$ . The high capacitance is due to the pre-intercalated Na<sup>+</sup> ions in the MnO<sub>2</sub> nanosheets. Furthermore, an asymmetric aqueous supercapacitor with Na<sub>3</sub>-MnO<sub>2</sub> positive and N-AC negative electrode was constructed, demonstrating a wide potential window of 2.4 V with a high energy density of  $64 \text{ Wh kg}^{-1}$  at a power density of  $1225 \text{ W kg}^{-1}$  and strong cycling stability of 83% capacitance retention. Our sample has a substantially greater content of pre-intercalated Na ions, which was prepared using a simple one-pot technique. Furthermore, the quick and effortless procedure, the low hydrothermal temperature, and the shorter time spent formulating our samples make the materials and process strong and significant in comparison to all the MnO<sub>2</sub>-based electrodes.



**Scheme 1.** Synthesis of Na-MnO<sub>2</sub>@CC.

## 2. Materials and Methods

All the chemical reagents were of analytical grade and used after purchase without any purification. All chemicals were Aladdin reagents and purchased from Shanghai Macklin Biochemical Co., Ltd., Shanghai, China.

The crystalline structures were characterized by Bruker D8 super speed X-ray diffractometer (XRD) with Cu K $\alpha$  radiation. The morphology of samples was observed with scanning electron microscopy (SEM) by (NAVO NanoSEM450 electron microscope FEI, USA), transmission electron microscopy (TEM) by JEOL 2010 transmission electron microscope, and high-resolution transmission electron microscope (HRTEM). Chemical characterization was performed by X-ray photoelectron spectroscopy (XPS) with an ESCALAB 250Xi spectrometer (Thermo Fisher, Loughborough, UK). Energy-dispersive X-ray spectroscopy (EDS) and HRTEM were used for elemental mapping.

### 2.1. Treatment of Carbon Cloth (CC)

CC was cut into a 4 cm  $\times$  2 cm rectangular strip, soaked, and sonicated in deionized water for 10 min. The CC was then sonicated in ethanol for 10 min. Acetone was used to repeat the process. Water, ethanol, and acetone were used to sonicate three times each. Finally, the carbon cloth was dried overnight at 60  $^{\circ}$ C in an oven.

### 2.2. Synthesis of Na<sub>3</sub>-MnO<sub>2</sub>

KMnO<sub>4</sub> (0.5 mmol, 0.079 g) and Na<sub>2</sub>SO<sub>4</sub> (21 mmol, 3 g) were dissolved using 50 mL of deionized water, and the solution was stirred for 1 h at room temperature. The clear solution was poured into a 100 mL PTFE liner enclosed by a stainless-steel autoclave, into which CC was placed afterward. The hydrothermal reaction took place at 120  $^{\circ}$ C for 1.5 h. The sample grown on the CC was rinsed three times with DI water and, finally, with ethanol. The mass loading of Na<sub>3</sub>-MnO<sub>2</sub> on the CC was 1.2 mg cm<sup>-2</sup>. Pure MnO<sub>2</sub> was produced using the same technique but without the addition of Na<sub>2</sub>SO<sub>4</sub>.

## 3. Results

The Na<sup>+</sup> pre-intercalated MnO<sub>2</sub> on CC was synthesized by a reasonably simple hydrothermal technique. To ensure structural integrity, the CC chosen as a substrate for growing samples prevented the addition of conductive additives and the polymer binder. CC, with its significant mechanical stability and flexibility, is a strong contender for binder-free electroactive material development [27,28].

Figure 1 shows an X-ray diffraction (XRD) investigation.  $\delta$ -MnO<sub>2</sub> (JCPDS card no.80-1098) can be given from the inset pattern because of the four main representative peaks detected at 12.4 $^{\circ}$ , 25 $^{\circ}$ , 37 $^{\circ}$ , and 65.5 $^{\circ}$  indexed with (001), (002), (111), and (020) having an interlayer spacing of 0.7  $\text{Å}$  [27,29]. The XRD patterns show the genesis of pure  $\delta$ -MnO<sub>2</sub>, but the low intensity and broadness of the peaks indicate the formation of nano-sized crystallites with poor crystallinity. There is no discernible change in the position of diffraction peaks

after the addition of Na ions, demonstrating that pre-intercalated Na<sup>+</sup> ions do not affect the crystal structure of MnO<sub>2</sub>.

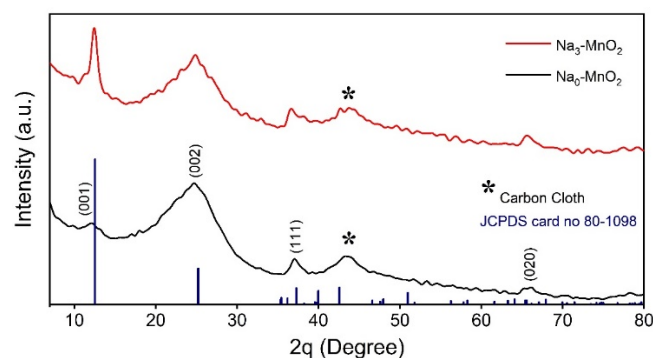


**Figure 1.** XRD patterns of Na<sub>0</sub>-MnO<sub>2</sub> and Na<sub>3</sub>-MnO<sub>2</sub>.

Field-emission scanning electron microscopy was used to observe the morphology and structure of all the Na<sub>3</sub>-MnO<sub>2</sub> samples. Figure 2 shows that the morphology did not change after the pre-intercalation of Na<sup>+</sup> to MnO<sub>2</sub>. Furthermore, high-magnification SEM images revealed that the Na<sub>3</sub>-MnO<sub>2</sub> is made up of ultra-thin uniform nanosheets of about a few nm thicknesses that are uniformly grown on the carbon cloth (Figure 2c). Nanosheets of Na<sub>0</sub>-MnO<sub>2</sub> (Figure 2c) are thicker than the nanosheets of Na<sub>3</sub>-MnO<sub>2</sub> (Figure 2f), which is thought to be helpful for ions insertion/extraction. The specific surface areas and electron-ion transfer distance affect the thickness of the nanosheet, which has a pronounced impact on the electrochemical properties of Na<sub>x</sub>-MnO<sub>2</sub> [30]. The EDS spectrum of Na<sub>3</sub>-MnO<sub>2</sub> is shown in Figure S1. The presence of the Na element in MnO<sub>2</sub> nanosheets can be seen in the elemental mapping of the energy-dispersive X-ray spectroscope in Figure S2. EDS analysis demonstrated that only Mn, Na, C, O, and K elements were present in the Na<sub>3</sub>-MnO<sub>2</sub>. This analysis proves that Na<sup>+</sup> ions successfully pre-intercalated and occupied the interlayer sites of the layered δ-MnO<sub>2</sub>.

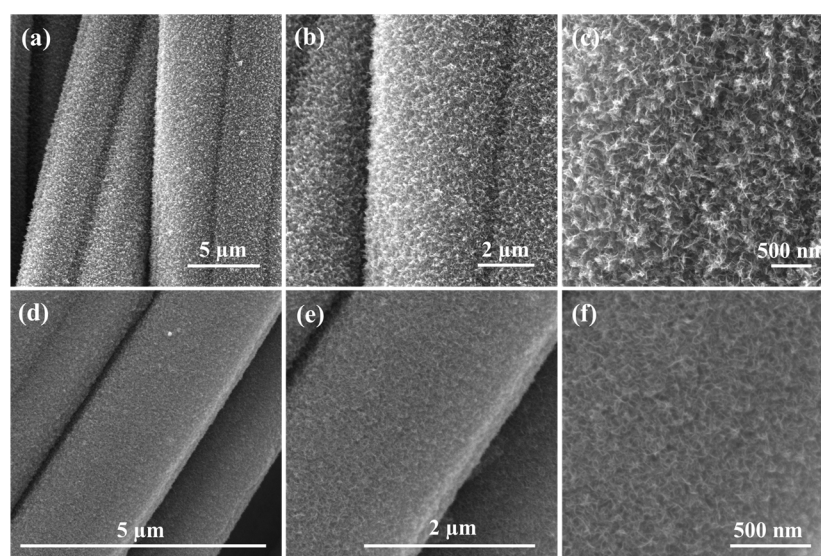


**Figure 2.** SEM images of Na<sub>0</sub>-MnO<sub>2</sub> (a–c); Na<sub>3</sub>-MnO<sub>2</sub> (d–f).

TEM analysis was used to investigate the structural details in greater depth and to assess the impact of the introduction of Na ions on the morphology of the Na<sub>3</sub>-MnO<sub>2</sub> electrode. Figure 3 depicts TEM representations of Na<sub>3</sub>-MnO<sub>2</sub> and MnO<sub>2</sub> electrodes with and without Na ions. The uniform MnO<sub>2</sub> nanostructures are composed of ultra-thin nanosheets, as shown in Figure 3a,c. The pre-intercalated Na ions decrease the grain size



of  $\text{MnO}_2$  nanosheets to a minuscule. Consequently, the active sites for ion adsorption are increased due to exceptional electrochemical performance. The creation of oxygen vacancies might emphasize the intrusion of electrolytes ions, leading to improved redox reaction and boosted conductivity. Figure 3b is the HRTEM image of  $\text{Na}_3\text{-MnO}_2$  nanosheets verifying the XRD data, as the lattice space in the central region is 0.7 nm, which correlates with the crystal plane (001) of  $\delta\text{-MnO}_2$ . The high-angle annular dark-field (HAADF) imaging in Figure 3e indicates a sustained arrangement of atomic species in the crystal phase of  $\text{MnO}_2$ , which also proves the presence of pre-intercalated Na ions in the layers of  $\delta\text{-MnO}_2$ .

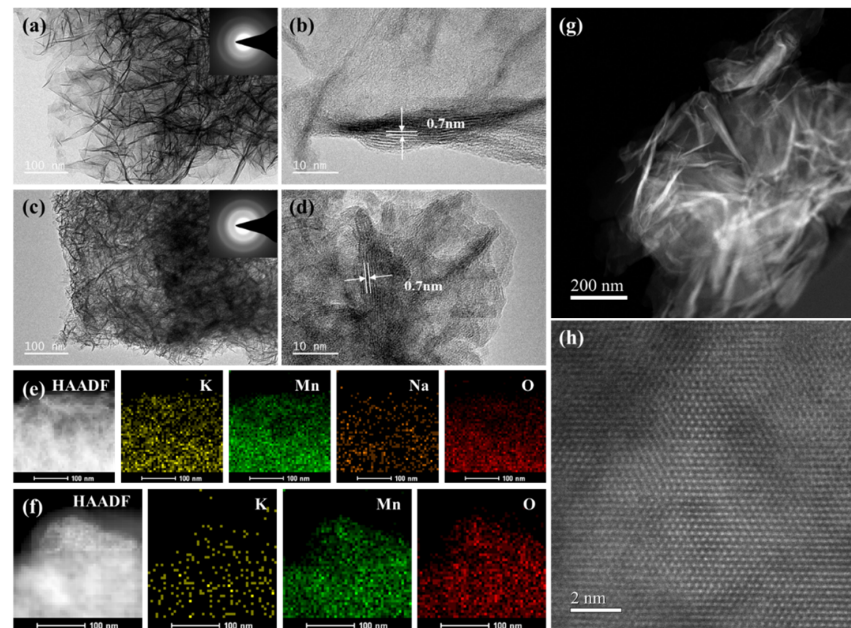


**Figure 3.** (a,c) TEM image of  $\text{Na}_3\text{-MnO}_2$ ; (b,d) HRTEM image of  $\text{Na}_3\text{-MnO}_2$ ; (e) elemental mapping of  $\text{Na}_3\text{-MnO}_2$ ; (f) elemental mapping of  $\text{MnO}_2$ ; (g,h) HAADF-STEM images.

Spherical aberration-corrected electron microscopy revealed the atomic resolution structure of the  $\text{Na}_3\text{-MnO}_2$  (Figure 3g,h). In Figure 3h, the white spots reflect the position of Mn atoms as seen from the  $\langle 001 \rangle$  zone axis.

The  $\text{Na}_3\text{-MnO}_2$  was analyzed by X-ray photoelectron spectroscopy (XPS). The survey spectrum shown in Figure 4a indicates the presence of C, O, Mn, and Na elements. Figure 4b reveals the high-resolution spectrum of Mn 2p. The peaks are pinpointed at binding energies of 642.3 eV and 654 eV, which correlate with the binding energies of Mn  $2p_{3/2}$  and Mn  $2p_{1/2}$ , respectively, with a difference of 11.7 eV. This stipulates that the oxidation state of Mn in the  $\text{Na}_3\text{-MnO}_2$  is +4, which is consistent with the previous literature [31–34]. Figure 4c shows high-resolution XPS spectra of Na 1s, which has a binding energy of 1071.4 eV [35–37]. It authenticates the successful intercalation of the  $\text{Na}^+$  into the  $\text{Na}_3\text{-MnO}_2$ .

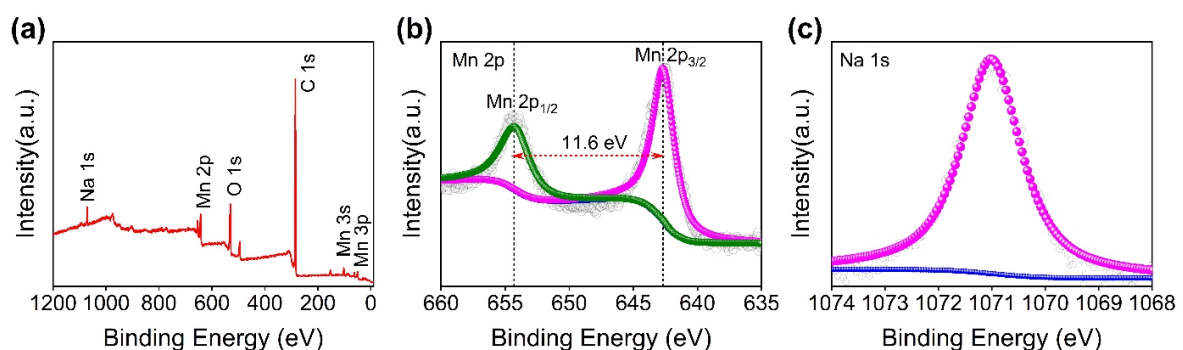


**Figure 4.** (a) Survey spectrum of  $\text{Na}_3\text{-MnO}_2$ ; (b) high-resolution spectrum of Mn 2p; (c) high-resolution spectrum of Na 1s.

To evaluate the electrochemical efficiency of the designed electrodes in a module of a three-electrode system, the electrochemical measurements were carried out on a VMP3 biologic workstation. This system consists of  $\text{Na}_0\text{-MnO}_2$  and  $\text{Na}_3\text{-MnO}_2$  as a working electrode and a Hg/HgO as a reference electrode and is completed with platinum foil as a counter electrode. We recorded the galvanostatic charge/discharge (GCD) measurements, electrochemical impedance spectroscopy (EIS), and cyclic voltammetry (CV) with 1M  $\text{Na}_2\text{SO}_4$  solution as the electrolyte.

Figure 5a displays the characteristics of CV curves of  $\text{Na}_3\text{-MnO}_2$  at the enlarged working potential range of 0–1.4 V at different scan rates (2, 5, 10, 20, and 50  $\text{mV s}^{-1}$ ). All the graphs represent a nearly rectangular shape comprising a noticeable redox peak at about 0.8 V. The current density increases correspondingly with the increase in scan rate, which is typical of  $\text{MnO}_2$ -based electrodes. By examining the CV curves of  $\text{Na}_3\text{-MnO}_2$  at varying potential ranges (Figure S3a), it is clear that the CV curves at 0–1.0 V potential range and various scan rates from 2 to 50  $\text{mV s}^{-1}$  have perfectly rectangular shapes at all scan rates with a small redox peak. Similarly, at 0–1.2 V, all the CV curves are rectangular, as shown in Figure S3b. However, a prominent pair of redox peaks is observed in the CV curves at 0–1.3 V (Figure S3d). The rectangular shape of enumerating the continuous and reversible faradaic redox transition with a pair of broad redox peaks at 0.4–0.6 V is noticeable in all the CV curves at all scan rates.

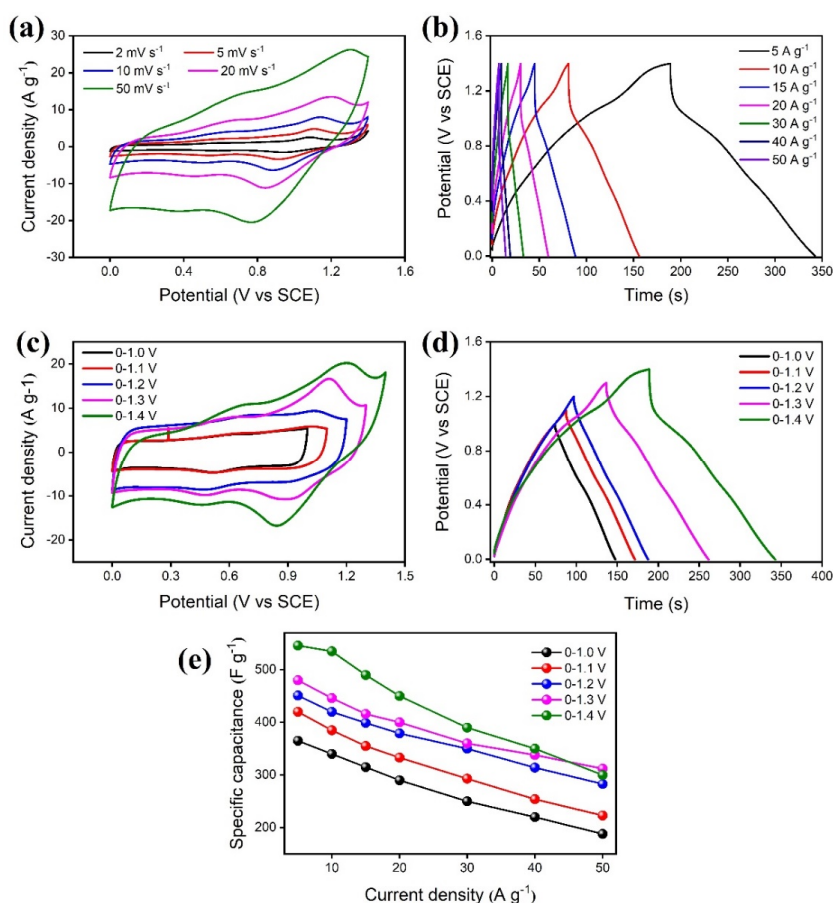


**Figure 5.** Electrochemical performance of  $\text{Na}_3\text{-MnO}_2$  electrode at potential range of 0–1.0, 0–1.1, 0–1.2, 0–1.3, and 0–1.4 V (a) CV curves at 2, 5, 10, 20, and 50  $\text{mV s}^{-1}$  scan rate and 0–1.4 V potential window; (b) GCD curves at 5, 10, 15, 20, 30, 40, and 50  $\text{A g}^{-1}$  current densities and 0–1.4 V potential window; (c) CV curves comparison at various potential ranges of 0–1.0, 0–1.1, 0–1.2, 0–1.3, and 0–1.4 V at a scan rate of 10  $\text{mV s}^{-1}$ ; (d) GCD curves comparison at different potential windows of 0–1.0, 0–1.1, 0–1.2, 0–1.3, and 0–1.4 V at 10  $\text{A g}^{-1}$  current density; (e) Specific capacitance comparison at various current densities of 5, 10, 15, 20, 30, 40, and 50  $\text{A g}^{-1}$  and 0–1.0, 0–1.1, 0–1.2, 0–1.3, and 0–1.4 V potential window.

Figure 5c shows the comparison of typical CV curves of the Na<sub>3</sub>-MnO<sub>2</sub> electrode at a scan rate of 10 mV s<sup>-1</sup> in varying potential windows of 0–1.4, 0–1.3, 0–1.2, 0–1.1, and 0–1.0 V, respectively. The CV curves of 0–1.0 and 1.1 V have an archetypal rectangular appearance with no redox peaks, which corresponds to the characteristic CV behavior for electrodes based on MnO<sub>2</sub> [38,39]. The CV curve developed a very small redox peak by escalating the potential range to 1.2 V. By further increasing the upper cutoff potential to 1.3 V, we observed a prominent couple of redox peaks at around ≈0.4 V. Upon further extending the potential window to 0–1.4 V, two pairs of redox peaks emerged: one at the lower potential range at about 0.4–0.6 V and the other at the higher potential range of about 0.8–1.2 V. The first redox peaks are due to the characteristic charge storage mechanism of MnO<sub>2</sub> by the intercalation and deintercalation of electrolytes on the Na<sub>3</sub>-MnO<sub>2</sub> electrode [40,41]. However, the mechanism of the second redox peak differs from that of the first, as stated by Nawishta J. et al. [42] and Gang L. et al. [43]. The CV curve area of Na<sub>3</sub>-MnO<sub>2</sub> at the 0–1.4 V potential window is much larger than that at 0–1.3, 0–1.2, 0–1.1, and 0–1.0 V. A reversible redox reaction causes the current to rise at around 1.0 V [44].

As one can observe, irrespective of the potential range, the CV graph exhibited a pair of distinguishing redox peaks at about 0.8 V for the anodic scanning and 1.2 V for the cathodic scanning at a potential range of 0–1.4 V, which appeared due to fast reversible redox reaction of the Mn<sup>3+</sup>/Mn<sup>4+</sup> plus the intercalation/deintercalation of the Na<sup>+</sup>. Remarkably, the potential windows sustain a fine rectangular shape even at a higher scan rate of 50 mV s<sup>-1</sup> and 0–1.4 V. This justifies the fact that due to the insertion of the Na<sup>+</sup>, the charging potential window rises noticeably [35]. It offers the prospect of designing SCs with a much higher energy density [45].

Figure 5b demonstrates the GCD curves at a potential range of 0–1.4 V and varying current densities (5, 10, 15, 20, 30, 40, and 50 A g<sup>-1</sup>). The fact that all of these curves are completely triangular confirms the pseudocapacitive existence of the Na<sub>3</sub>-MnO<sub>2</sub> electrode. The GCD curves at 0–1.0 V, 0–1.1 V, 0–1.2 V, and 0–1.3 V at current densities of 5, 10, 15, 20, 30, 40, 50, 80, and 100 A g<sup>-1</sup> are shown in Figure S4a–d, respectively. Figure 5d shows a comparison of GCD curves at 5 A g<sup>-1</sup> current density at various potential ranges of 0–1.0, 0–1.1, 0–1.2, 0–1.3, and 0–1.4 V. Among these curves, the GCD curves at 0–1.4 V show a longer charge–discharge time. The charge–discharge time declined as the current density increased due to the reduced passage of electrolyte ions across the electrode [33]. Still, at a higher current density of 100 A g<sup>-1</sup>, the nanocomposite MnO<sub>2</sub> electrode displayed a linear triangular shape, demonstrating that the pre-intercalation of Na<sup>+</sup> leads to superlative electrochemical performance.

Figure 5e expresses a comparative analysis of specific capacitance of Na<sub>3</sub>-MnO<sub>2</sub> at various potential windows (0–1.0, 0–1.1, 0–1.2, 0–1.3, and 0–1.4 V) as a function of current density. The specific capacitance of the Na<sub>3</sub>-MnO<sub>2</sub> electrode at a potential window of 0–1.4 V can reach 546, 535, 490, 450, 390, 350, and 300 F g<sup>-1</sup> at 5, 10, 15, 20, 30, 40, and 50 A g<sup>-1</sup>, respectively, which surpasses that of 480 F g<sup>-1</sup> at the potential window of 0–1.3 V and is far better than 451 F g<sup>-1</sup> at the potential window of 0–1.2 V at 5 A g<sup>-1</sup> current density. The specific capacitance of the Na<sub>3</sub>-MnO<sub>2</sub> electrode is much higher than the recently published work based on MnO<sub>2</sub> electrodes, such as δ-MnO<sub>2</sub> (251.4 F g<sup>-1</sup> at current density 1 A g<sup>-1</sup>) [46], δ-MnO<sub>2</sub> NFs@α-MnO<sub>2</sub> NWs (310 F g<sup>-1</sup> at current density 1 A g<sup>-1</sup>) [47], MnO<sub>2</sub>@SBA-C (219 F g<sup>-1</sup> at current density 1 A g<sup>-1</sup>) [48], 3D-HPCS@MnO<sub>2</sub> (231.5 F g<sup>-1</sup> at current density 1 A g<sup>-1</sup>) [49], δ-MnO<sub>2</sub> (194.3 F g<sup>-1</sup> at current density 1 A g<sup>-1</sup>) [50], NSs@MnO<sub>2</sub> HNPs (244.54 F g<sup>-1</sup> at current density 1 A g<sup>-1</sup>) [51], α-MnO<sub>2</sub>@δ-MnO<sub>2</sub> (206 F g<sup>-1</sup> at current density 1 A g<sup>-1</sup>) [52], and rGO/CNT/MnO<sub>2</sub> (209 F g<sup>-1</sup> at current density 1 A g<sup>-1</sup>) [53]. At the same current density, the specific capacitance of the Na<sub>3</sub>-MnO<sub>2</sub> electrode at the potential window of 0–1.1 and 0–1.0 V is 420 and 365 F g<sup>-1</sup>, respectively.

To comprehensively understand the stability of Na<sub>3</sub>-MnO<sub>2</sub> electrodes in different potential ranges, the cycle stability of Na<sub>3</sub>-MnO<sub>2</sub> is analyzed and correlated at a current density of 10 A g<sup>-1</sup> over 6000 cycles and is shown in Figure S11. The Na<sub>3</sub>-MnO<sub>2</sub> electrode has a capacitance retention of 95, 93, 94, and 96% in different working potential windows of 0–1.1, 0–1.2, 0–1.3, and 0–1.4, respectively. Noticeably, extending the potential window to 0–1.4 V has

good cycling stability, which could be explained by the pre-intercalated  $\text{Na}^+$  in the  $\text{Na}_3\text{-MnO}_2$  structure as a result of charge balancing, which acts as pillars to stabilize the nanosheets' layered structures. The electrochemical performance of pure  $\text{MnO}_2$  was recorded to upgrade the understanding of the pre-intercalation of  $\text{Na}^+$  into  $\text{MnO}_2$  and its effect on the electrochemical behavior of the  $\text{Na}_3\text{-MnO}_2$  electrode. Figure S6 shows the CV of the  $\text{MnO}_2$  electrode at a scan rate of 1, 2, 5, 10, 20, 50, and  $100 \text{ mV s}^{-1}$  in different working potential windows of 0–1.0 (Figure S6a), 0–1.2 (Figure S6c), and 0–1.4 V (Figure S6e), respectively. It is obvious that no redox peaks polarization occurred when the potential window exceeded 1 V. The current density of the CV curve was observed to be increased as the potential window was increased, without any observable redox peaks for all potential ranges. Furthermore, the CV curve of  $\text{MnO}_2$  at a potential range of 0–1.4 showed water decomposition with the evolution of oxygen. In addition, the area under the CV curve for  $\text{Na}_3\text{-MnO}_2$  is larger than the current density of  $\text{MnO}_2$  at all potential windows. Similarly, the GCD analysis of  $\text{MnO}_2$  electrodes at different potential windows of 0–1.0 (Figure S6b), 0–1.2 (Figure S6d), and 0–1.4 V (Figure S6f) at various current densities of 1, 2, 5, 10, 15, 20, 30, 40, 50, 80, and  $100 \text{ A g}^{-1}$  showed different results to  $\text{Na}_3\text{-MnO}_2$ . The most important point is that it did not even reach the potential window of 1.4 V. The GCD curves of  $\text{Na}_3\text{-MnO}_2$  are more symmetric than those of  $\text{MnO}_2$ , indicating the better reversibility of  $\text{Na}_3\text{-MnO}_2$  electrode than that of the  $\text{MnO}_2$ . Moreover, the discharge time of the  $\text{Na}_3\text{-MnO}_2$  electrode is much longer than the pure  $\text{MnO}_2$  electrode, indicating higher capacitance of the  $\text{Na}_3\text{-MnO}_2$  electrode. These results indicate that the pre-intercalation of  $\text{Na}^+$  can increase the capacitance performance and extend the stable potential window of  $\text{MnO}_2$  [54].

Similarly, Figure S7 compares the specific capacitance of the  $\text{MnO}_2$  electrode as a function of current density at various potential ranges of 0–1.0, 0–1.2, and 0–1.4 V.  $\text{MnO}_2$  has a very low specific capacitance relative to the  $\text{Na}_3\text{-MnO}_2$  electrode at all current densities. The highest recorded specific capacitance was noted to be  $217 \text{ F g}^{-1}$  at a current density of  $1 \text{ A g}^{-1}$  and a potential window of 1.4 V.

To test the applicability of the electrochemical performances of the  $\text{Na}_3\text{-MnO}_2$  electrode in a full device for a wide potential window, an aqueous  $\text{Na}_3\text{-MnO}_2//\text{N-AC}$  device was engineered with a  $\text{Na}_3\text{-MnO}_2$  electrode as the positive electrode (cathode) and commercial N-doped activated carbon (N-AC) electrode as the negative electrode (anode), completing this device with 1 M  $\text{Na}_2\text{SO}_4$  solution as aqueous electrolyte. Before measuring the electrochemical performance of the  $\text{Na}_3\text{-MnO}_2//\text{N-AC}$  device, the electrochemical performance of N-AC was analyzed, as shown in Figure S8.

Figure S9a depicts the CV curves for the  $\text{Na}_3\text{-MnO}_2$  electrode and the N-AC in their respective potential windows of 1.4–0 V and 0–1.0 V at a scan rate of  $10 \text{ mV s}^{-1}$ . Theoretically, it is clear from the separate potential window of cathode and anode that the  $\text{Na}_3\text{-MnO}_2//\text{N-AC}$  device could accomplish the working potential window of 0–2.4 V. To experimentally optimize the highest possible upper cutoff voltage for the  $\text{Na}_3\text{-MnO}_2//\text{N-AC}$  device, CV curves were reported at different potential windows from 1.6 to 2.6 V at a scan rate of  $10 \text{ mV s}^{-1}$ , as shown in Figure S9b. As the potential window of the  $\text{Na}_3\text{-MnO}_2//\text{N-AC}$  device extended beyond 0–2.4 V, a distinct current leap began to appear at a potential window of about 0–2.6 V, indicating the decomposition of the water started here. Notably, the CV curves of the  $\text{Na}_3\text{-MnO}_2//\text{N-AC}$  device could sustain a quasi-rectangular shape with potential windows ranging from 0 to 2.4 V, confirming the maximum potential window for the  $\text{Na}_3\text{-MnO}_2//\text{N-AC}$  device could reach as high as 2.4 V without any aqueous electrolyte decomposition.

To adjust the electrochemical performance of the  $\text{Na}_3\text{-MnO}_2//\text{N-AC}$  device, the mass ratio of the cathode to the anode was calculated to be 1.2:3.4, based on the charge balance theory (Equation (1)), at a current density of  $1 \text{ A g}^{-1}$ . The electrochemical performance of the  $\text{Na}_3\text{-MnO}_2//\text{N-AC}$  device is shown in Figure 6.



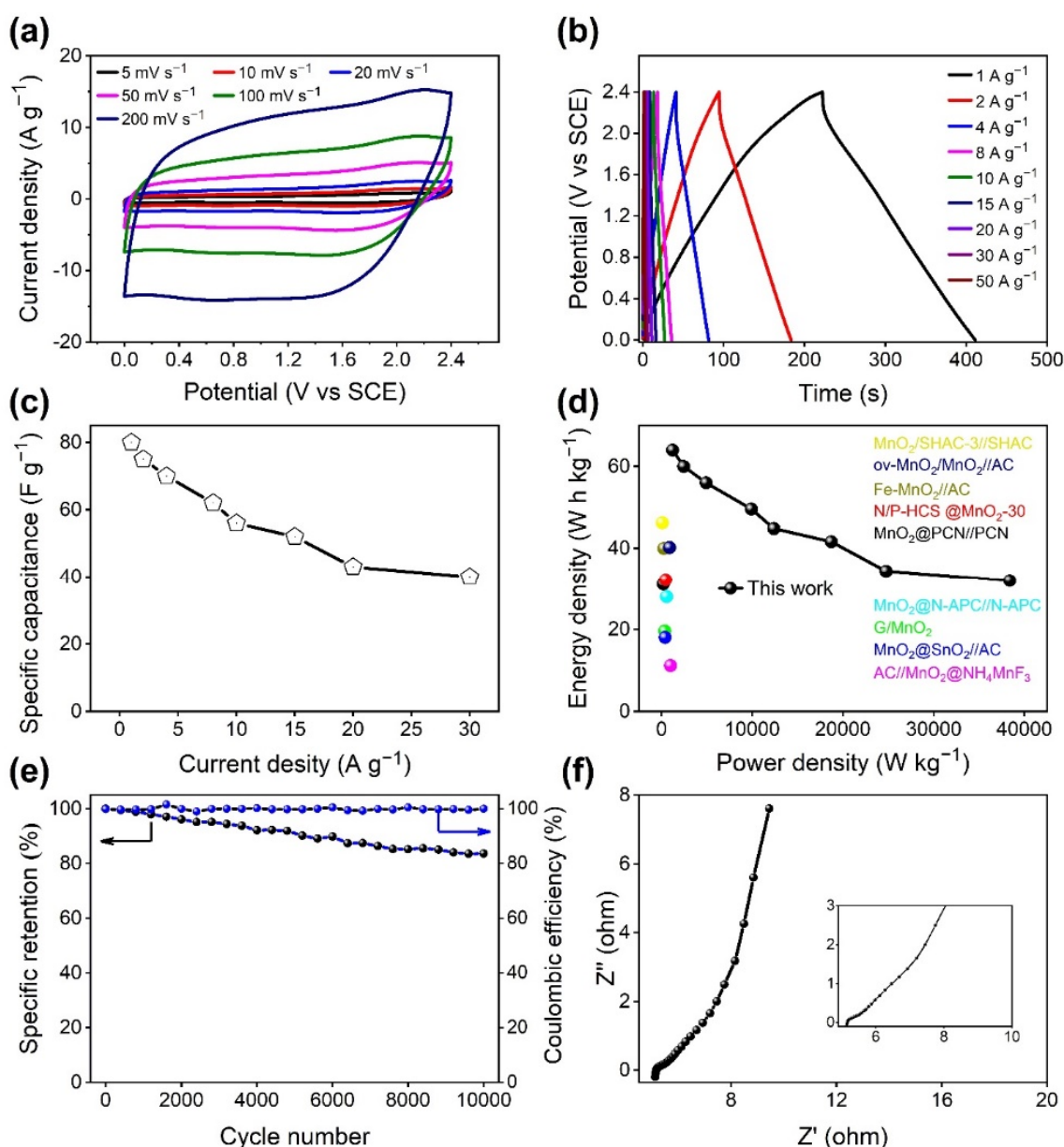


**Figure 6.** Electrochemical performance of Na<sub>3</sub>-MnO<sub>2</sub>//N-AC device (a) CV curves at 5, 10, 20, 50, 100, and 200 mV s<sup>-1</sup> scan rate and 0–2.4 V potential window; (b) GCD curves at 1, 2, 4, 8, 10, 15, 20, 30, and 50 A g<sup>-1</sup> current densities and 0–2.4 V potential window; (c) Specific capacitance at various current densities of 1, 2, 4, 8, 10, 15, 20, and 30 A g<sup>-1</sup> current densities (d) Ragone plot of the gravimetric energy density and power density comparison of this work Na<sub>3</sub>-MnO<sub>2</sub>//N-AC device and other previously reported works; (e) The cycling stability and Coulombic efficiency at 10 A g<sup>-1</sup>; (f) EIS.

CV curves of Na<sub>3</sub>-MnO<sub>2</sub>//N-AC device at various scan rates (5, 10, 20, 50, 100, and 200 mV s<sup>-1</sup>) in a wide (0–2.4 V) potential window were recorded and shown in Figure 6a. Interestingly, the quasi-rectangular shape of the CV curve was preserved at an even higher scan rate of 200 mV s<sup>-1</sup>, exhibiting the exceptional electrochemical characteristics of the Na<sub>3</sub>-MnO<sub>2</sub>//N-AC device. GCD measurements were used to further investigate the electrochemical properties of Na<sub>3</sub>-MnO<sub>2</sub>//N-AC device at 1, 2, 4, 8, 10, 15, 20, 30, and 50 A g<sup>-1</sup> current densities and 0–2.4 V potential window (Figure 6b). All these GCD curves displayed quasi-triangular shape and good symmetry, confirming the ideal super capacitive behavior of the Na<sub>3</sub>-MnO<sub>2</sub>//N-AC device. From these GCD curves, the specific capacitances for the Na<sub>3</sub>-MnO<sub>2</sub>//N-AC device were calculated and are represented in

Figure 6c. Fascinatingly, the Na<sub>3</sub>-MnO<sub>2</sub>//N-AC device has the highest specific capacitance of 80 F g<sup>-1</sup> at a current density of 1 A g<sup>-1</sup> and can retain 50% of its capacitance even at a high current density of 30 A g<sup>-1</sup>, indicating the excellent rate capability of the device.

According to Equations (1) and (2), the Na<sub>3</sub>-MnO<sub>2</sub>//N-AC device demonstrated the highest energy of 64 Wh kg<sup>-1</sup> at the power density of 1225.53 W kg<sup>-1</sup>. This device maintained a higher energy density of 32 Wh kg<sup>-1</sup> at a current density of 30 A g<sup>-1</sup> even at the highest power density of 38400 W kg<sup>-1</sup> (Figure 6d). These high-energy and power densities outperform those of recently published Mn-based devices, such as MnO<sub>2</sub>@PCN//PCN (energy density 31.13 Wh kg<sup>-1</sup>, at power density 193.6 W kg<sup>-1</sup>) [55], N/P-HCS@MnO<sub>2</sub>-30 (energy density 32.21 Wh kg<sup>-1</sup>, at power density 449.8 W kg<sup>-1</sup>) [43], G/MnO<sub>2</sub> (energy density 19.6 Wh kg<sup>-1</sup>, at power density 351 W kg<sup>-1</sup>) [56], MnO<sub>2</sub>@SnO<sub>2</sub>//AC (energy density 18.05 Wh kg<sup>-1</sup>, 403.6 W kg<sup>-1</sup>) [57], MnO<sub>2</sub>@N-APC//N-APC (energy density 28 Wh kg<sup>-1</sup>, at power density 560 W kg<sup>-1</sup>) [58], AC//MnO<sub>2</sub>@NH<sub>4</sub>MnF<sub>3</sub> (energy density 11.2 Wh kg<sup>-1</sup>, at power density 1000 W kg<sup>-1</sup>) [59], MnO<sub>2</sub>/SHAC-3//SHAC (energy density 46.2 Wh kg<sup>-1</sup>, at power density 98.5 W kg<sup>-1</sup>) [60], Fe-MnO<sub>2</sub>//AC (energy density 40 Wh kg<sup>-1</sup>, at power density 250 W kg<sup>-1</sup>) [61], and ov-MnO<sub>2</sub>@MnO<sub>2</sub>//AC (energy density 40.2 Wh kg<sup>-1</sup>, at power density 891.2 W kg<sup>-1</sup>) [62]. Furthermore, the quick and effortless procedure, low hydrothermal temperature, and shorter time spent formulating our samples make the materials and process strong and significant versus all the MnO<sub>2</sub>-based electrodes.

Figure S10 shows the results of the volumetric energy and power density calculations. The Na<sub>3</sub>-MnO<sub>2</sub>//N-AC device delivered excellent volumetric energy and power density (12.8 Wh cm<sup>-3</sup> at 245 W cm<sup>-3</sup>). Cycling performance is another very important parameter used to check the stability of the device. As noticed in Figure 6e, the cycling performance of the Na<sub>3</sub>-MnO<sub>2</sub>//N-AC device was recorded under a current density of 10 A g<sup>-1</sup> for 10,000 cycles at a 2.4 V potential window. As seen in the graph, the device retained 83% of capacitance, confirming its outstanding cycling durability. Pre-intercalation could markedly mitigate these capacity fading concerns caused by structural instabilities during cycling because of the limited volumetric variability during the intercalation/de-intercalation phase of the carrier ions.

The EIS results of the Na<sub>3</sub>-MnO<sub>2</sub>//N-AC device are illustrated in Figure 6f, with a semicircle at a higher-frequency and a straight line at a lower-frequency region.

The electrochemical performance of Na ions pre-intercalated MnO<sub>2</sub> was improved in this study. The most likely reasons are as follows. A broader interlayer space is particularly favorable for the intercalation–deintercalation of various ions during the redox process, which is given by wide interlayers of MnO<sub>2</sub>. The lattice space in the central region of the Na<sub>3</sub>-MnO<sub>2</sub> nanosheets is 0.7 nm, which matches with the crystal plane (001) of δ-MnO<sub>2</sub>, as revealed by the HRTEM image, which supports the XRD results. The electrochemically active sites were increased due to the morphology with very thin nanosheets, which helped reduce the electron transport channel and the diffusion pathway of the ions of electrolyte, which optimized the electrochemical performance. Furthermore, the pre-intercalation of Na ions shrinks the nanosheets and disrupts the lattice alignment, as seen in the SEM images, resulting in a large turnout of grain borders. These numerous grain boundaries provide more active sites for redox reactions, as well as a simple diffusion pathway for ions and electrons, allowing the electrode materials to be used more competently. Furthermore, greater grain boundaries stimulate the formation of lattice defects, which increase the number of oxygen vacancies and so refine the electrical conductivity of Na<sub>3</sub>-MnO<sub>2</sub>.

#### 4. Computational Studies

The present study was performed by implementing the density functional theory (DFT) using the generalized gradient approximation (GGA) and the Perdew–Burke–Ernzerhof (PBE)59 functional for the exchange correlation potentials that were accomplished through the Vienna ab initio simulation package (VASP)60–62. The structure was optimized using 8 × 6 × 4 k-points, and a 520 eV energy cutoff was applied. The electronic properties of bulk MnO<sub>2</sub> were calculated using Dudarev’s PBE+U method [63], with U = 3.9 eV applied

to the 3d states of each Mn atom. The  $U = 3.9$  eV for Mn is also reported in the previous literature study [64,65]. Furthermore, the high symmetry and denser  $16 \times 12 \times 10$  k-points were used for the calculations of the bandstructure and density of states.

The  $\text{MnO}_2$  was modeled via a periodic cell containing 12 atoms (4 manganese and 8 oxygen atoms). The  $\text{MnO}_2$  supercell was orthorhombic  $2.92 \times 4.58 \times 9.43$  Å<sup>3</sup> for the x, y, and z-directions, with  $\alpha = \beta = \gamma = 90^\circ$ , and the periodic condition was employed along the x, y, and z directions. The total energy was converged to an accuracy of  $1 \times 10^{-5}$  eV to obtain accurate forces, and a force tolerance of  $-0.02$  eV/Å was applied in the structure optimization. The d orbital of manganese, p orbital of oxygen, and s orbital of Na hybridize, which results in the crowding of bands near the Fermi level in Na-intercalated hybrid structures c and d, exhibiting band gap reduction, which assists in charge transportation.

Figure 7c also exhibits the affinity between Na and oxygen of manganese oxide, therefore concluding that the intercalation of sodium is due to strong bonding between oxygen and sodium atoms.

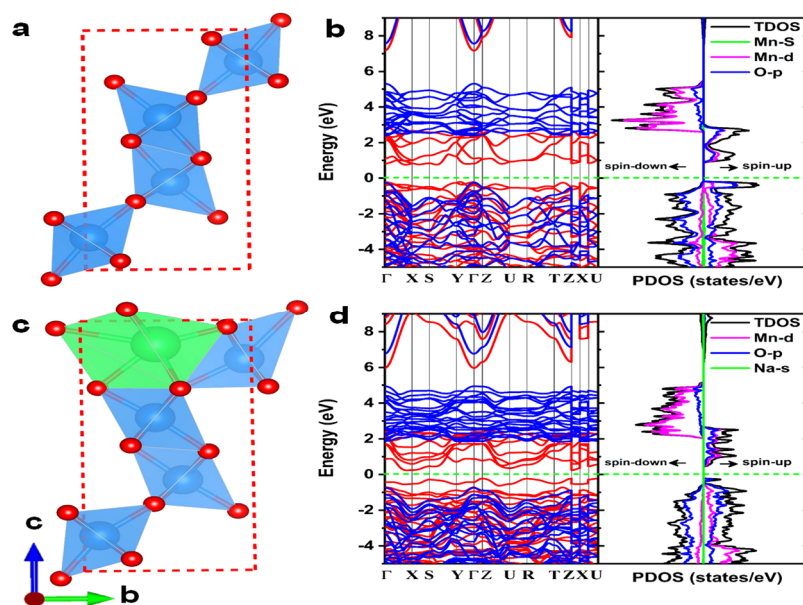


**Figure 7.** The electronic band structure, the spin-polarized total density of states (TDOS), and partial density of states (PDOS) plotted together with corresponding optimized structures of (a,b) pure  $\text{MnO}_2$ ; and (c,d) Na-doped  $\text{MnO}_2$ ; The spin-up ( $\uparrow$ ) and spin-down ( $\downarrow$ ).

To analyze the charge transfer and charge population, Figure 8, bader charge calculations were performed according to the following equation.

$$\text{Work function} = \text{Vacuum potential } (E_{\text{vac}}) - \text{Fermi Level } (E_f) \quad (1)$$

The charge density difference ( $\Delta\rho$ ) was calculated as

$$\Delta\rho = \rho_{\delta - \text{MnO}_2} - \rho_{\text{Na}}$$

where  $\rho_{\delta - \text{MnO}_2}$ ,  $\rho_{\text{Na}}$  represents the charge densities of  $\delta - \text{MnO}_2$  and Na-pre-intercalated  $\delta - \text{MnO}_2$ .

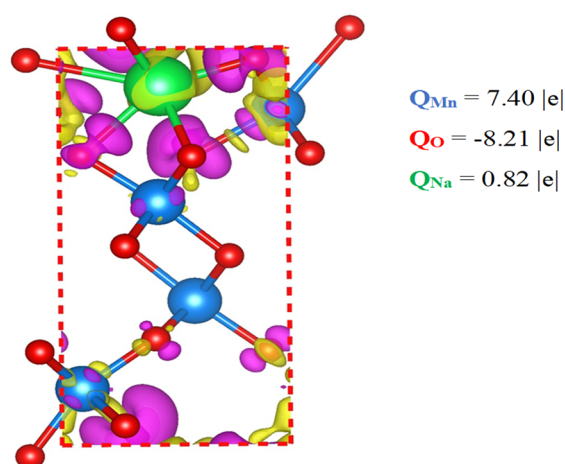


**Figure 8.** The charge density difference plot of Na-doped  $\text{MnO}_2$ . The violet and yellow colors specify electron accumulation and depletion regions, respectively. The red, bluish, and green colors balls represent O, Mn, and Na atoms, respectively. The iso-surface value is set to  $0.002 \text{ e Bohr}^{-3}$ .

The zero-point energy, entropy, and enthalpy corrections were added to the adsorbates to convert electronic energy to free energy. The Gibbs free energy ( $G$ ) at 0 V is modified by Equation (2)

$$G = E_{\text{DFT}} + E_{\text{ZPE}} - TS + \int C_p dT \quad (2)$$

where  $E_{\text{DFT}}$ ,  $E_{\text{ZPE}}$ ,  $TS$ , and  $\int C_p dT$  denote the electronic energy obtained from DFT optimization, zero-point vibrational energy, entropy, and heat capacity at room temperature.

The bader charge calculations prove that  $7.40 |e|$  electrons are transferred from manganese to sodium, which may assist in the intercalation/de-intercalation process.

## 5. Conclusions

In conclusion, we designed  $\text{Na}^+$  pre-intercalated  $\text{MnO}_2$  for high-performance supercapacitors with a potential range of 0–1.4 V. The potential window of the  $\text{Na}_3\text{-MnO}_2$  electrode can reach up to 1.4 V versus Hg/HgO. As a result, the  $\text{Na}_3\text{-MnO}_2$  electrode has a high specific capacitance of  $546 \text{ F g}^{-1}$  and good rate capability. It demonstrated exceptional cycling stability with nearly 95% retention of the capacitance after 6000 cycles at  $10 \text{ A g}^{-1}$  at 1.4 V. Furthermore, the  $\text{Na}_3\text{-MnO}_2$  // N-AC device with  $\text{Na}_3\text{-MnO}_2$  as positive and N-AC as negative electrodes demonstrated superior electrochemical performance with a wider potential window (0–2.4 V) and higher energy and power densities ( $64 \text{ Wh kg}^{-1}$  at  $1225.53 \text{ W kg}^{-1}$ ), as well as excellent long-term cycling stability (83% capacitance retention after 10,000 cycles). This technique aims to bring new insights into the goal of a simple nanostructure, potentially leading to novel supercapacitor designs with longer working potential windows, more energy, and improved power density.

**Supplementary Materials:** The following supporting information can be downloaded at: <https://www.mdpi.com/article/10.3390/nano12162856/s1>, Figure S1: EDS elemental mapping of  $\text{Na}_3\text{-MnO}_2$ ; Figure S2. EDS mapping of  $\text{Na}_3\text{-MnO}_2$ ; Figure S3. The CV of  $\text{Na}_3\text{-MnO}_2$  at a scan rate of 1, 2, 5, 10, 20, and  $50 \text{ mV s}^{-1}$  in different working potential windows of (a) 0–1.0 V (b) 0–1.1 V; (c) 0–1.2 V; and (d) 0–1.3 V; Figure S4. The GCD of  $\text{Na}_3\text{-MnO}_2$  at various current densities of 5, 10, 15, 20, 30, 40, 50, 80 and  $100 \text{ A g}^{-1}$  in different working potential windows of (a) 0–1.0 V (b) 0–1.1 V; (c) 0–1.2 V; and (d) 0–1.3 V; Figure S5. Nyquist plots recorded at 100 kHz to 10 MHz of  $\text{Na}_3\text{-MnO}_2$  at different working potential windows; Figure S6. Electrochemical performance of the of  $\text{MnO}_2$  without Na ions; CV at a scan rate of 1, 2, 5, 10, 20, 50 and  $100 \text{ mV s}^{-1}$  in different working potential windows (a) 0–1.0 V; (c) 0–1.2 V; (e) 0–1.4 V; GCD curves at a various current density of 1, 2, 5, 10, 15, 20, 30, 40, 50, 80 and  $100 \text{ A g}^{-1}$  in different working potential windows of (b) 0–1.0 V; (d) 0–1.2 V and (f) 0–1.4 V; Figure S7. comparison of specific capacitance of  $\text{MnO}_2$  electrode at different potential window of 0–1.0, 0–1.2, and 0–1.4 V as function of current density; Figure S8. the electrochemical performance of AC was recorded



in the three-electrode system; (a) CV of the at a scan rate of 10–200 mV s<sup>-1</sup> in 0–1.0 V; (b) GC of the at a current density of 1–20 A g<sup>-1</sup> in 0–1.0 V; (c) specific capacitance as a function of current density; Figure S9. Comparison of CV curves of Na<sub>3</sub>-MnO<sub>2</sub> electrode and N-AC in their separate potential windows of 1.4–0 V and 0–1.0 V respectively at a scan rate of 10 mV s<sup>-1</sup>; (b) CV curves at different potential windows from 1.6 to 2.6 V were recorded at a scan rate of 10 mV s<sup>-1</sup>; Figure S10. Ragone plots of Na<sub>3</sub>-MnO<sub>2</sub>/N-AC device volumetric energy and power density; Figure S11. Cycling performance comparison at potential window of 0–1.0, 0–1.1, 0–1.2, 0–1.3, and 0–1.4 V.

**Author Contributions:** A.U.R. and W.J. designed the project. A.U.R. and N.Z. performed the experiments. A.U.R. and N.Z. analyzed the data and wrote the manuscript. A.A. and G.L. critically reviewed the manuscript. G.L. supervised and rechecked the manuscript. M.T., S.U., and M.S. performed the DFT. All authors have read and agreed to the published version of the manuscript.

**Funding:** This research was supported by National Natural Science Foundation of China, award number 91956110, 22071102, 11911530174 and the Robert A. Welch Foundation (D-1361-20210327, USA).

**Institutional Review Board Statement:** Not applicable.

**Informed Consent Statement:** Not applicable.

**Data Availability Statement:** The data are available on reasonable request from the corresponding author.

**Conflicts of Interest:** The authors declare no conflict of interest.

## References

1. Song, Z.; Miao, L.; Ruhlmann, L.; Lv, Y.; Zhu, D.; Li, L.; Gan, L.; Liu, M. Self-assembled carbon superstructures achieving ultra-stable and fast proton-coupled charge storage kinetics. *Adv. Mater.* **2021**, *33*, 2104148. [[CrossRef](#)] [[PubMed](#)]
2. Muzaffar, A.; Basheer Ahamed, M.; Deshmukh, K. Nature-Inspired Electrodes for Flexible Supercapacitors. In *Flexible Supercapacitor Nanoarchitectonics*; Wiley: Hoboken, NJ, USA, 2021; pp. 549–573. [[CrossRef](#)]
3. Shi, Z.; Sun, G.; Yuan, R.; Chen, W.; Wang, Z.; Zhang, L.; Zhan, K.; Zhu, M.; Yang, J.; Zhao, B. Scalable fabrication of NiCo<sub>2</sub>O<sub>4</sub>/reduced graphene oxide composites by ultrasonic spray as binder-free electrodes for supercapacitors with ultra-long lifetime. *J. Mater. Sci. Technol.* **2022**, *99*, 260–269. [[CrossRef](#)]
4. Zarshad, N.; Wu, J.; Rahman, A.U.; Ali, A.; Qiu, C.; Aisha, R.; Gao, R.; Xie, Y.; Ni, H. Binder and conductive agent-free electrode for the excellent aqueous asymmetrical supercapacitor. *Solid State Sci.* **2021**, *112*, 106530. [[CrossRef](#)]
5. Sun, G.; Ren, H.; Shi, Z.; Zhang, L.; Wang, Z.; Zhan, K.; Yan, Y.; Yang, J.; Zhao, B. V<sub>2</sub>O<sub>5</sub>/vertically-aligned carbon nanotubes as negative electrode for asymmetric supercapacitor in neutral aqueous electrolyte. *J. Colloid Interface Sci.* **2021**, *588*, 847–856. [[CrossRef](#)]
6. Salanne, M.; Rotenberg, B.; Naoi, K.; Kaneko, K.; Taberna, P.-L.; Grey, C.P.; Dunn, B.; Simon, P. Efficient storage mechanisms for building better supercapacitors. *Nat. Energy* **2016**, *1*, 16070. [[CrossRef](#)]
7. Choi, C.; Ashby, D.S.; Butts, D.M.; DeBlock, R.H.; Wei, Q.; Lau, J.; Dunn, B. Achieving high energy density and high power density with pseudocapacitive materials. *Nat. Rev. Mater.* **2020**, *5*, 5–19. [[CrossRef](#)]
8. Huang, J.; Yuan, K.; Chen, Y. Wide Voltage Aqueous Asymmetric Supercapacitors: Advances, Strategies, and Challenges. *Adv. Funct. Mater.* **2021**, *32*, 2108107. [[CrossRef](#)]
9. Rahman, A.U.; Zarshad, N.; Wu, J.; Faiz, F.; Raziq, F.; Ali, A.; Li, G.; Ni, H. Fabrication of Ag-doped MnO<sub>2</sub> nanosheets@carbon cloth for energy storage device. *Mater. Sci. Eng. B* **2021**, *269*, 115150. [[CrossRef](#)]
10. Zarshad, N.; Rahman, A.U.; Wu, J.; Ali, A.; Raziq, F.; Han, L.; Wang, P.; Li, G.; Ni, H. Enhanced energy density and wide potential window for K incorporated MnO<sub>2</sub>@carbon cloth supercapacitor. *Chem. Eng. J.* **2021**, *415*, 128967. [[CrossRef](#)]
11. Zarshad, N.; Wu, J.; Rahman, A.U.; Tariq, M.; Ali, A.; Ni, H. MnO<sub>2</sub> nanospheres electrode composed of low crystalline ultra-thin nanosheets for high performance and high rate supercapacitors. *Mater. Sci. Eng. B* **2020**, *259*, 114610. [[CrossRef](#)]
12. Zarshad, N.; Wu, J.; Rahman, A.U.; Yu, H.; Ali, A.; Ni, H. Green and environmental-friendly method to synthesize template free nano grass-flower hierarchical manganese dioxide for high performance supercapacitor. *Solid State Sci.* **2020**, *106*, 106138. [[CrossRef](#)]
13. Ghosh, S.K. Diversity in the family of manganese oxides at the nanoscale: From fundamentals to applications. *ACS Omega* **2020**, *5*, 25493–25504. [[CrossRef](#)] [[PubMed](#)]
14. Ma, N.; Kosasang, S.; Krittayavathananon, A.; Phattharasupakun, N.; Sethuraman, S.; Sawangphruk, M. Effect of intercalated alkali ions in layered manganese oxide nanosheets as neutral electrochemical capacitors. *Chem. Commun.* **2019**, *55*, 1213–1216. [[CrossRef](#)]
15. Du, W.; Miao, L.; Song, Z.; Zheng, X.; Lv, Y.; Zhu, D.; Gan, L.; Liu, M. Kinetics-driven design of 3D VN/MXene composite structure for superior zinc storage and charge transfer. *J. Power Sources* **2022**, *536*, 231512. [[CrossRef](#)]
16. He, S.; Mo, Z.; Shuai, C.; Liu, W.; Yue, R.; Liu, G.; Pei, H.; Chen, Y.; Liu, N.; Guo, R. Pre-intercalation  $\delta$ -MnO<sub>2</sub> Zinc-ion hybrid supercapacitor with high energy storage and Ultra-long cycle life. *Appl. Surf. Sci.* **2022**, *577*, 151904. [[CrossRef](#)]

17. Vedpathak, A.S.; Desai, M.A.; Bhagwat, S.; Sartale, S.D. Green strategy for the synthesis of  $K^+$  pre-inserted  $MnO_2/rGO$  and its electrochemical conversion to  $Na-MnO_2/rGO$  for high-performance supercapacitors. *Energy Fuels* **2022**, *36*, 4596–4608. [[CrossRef](#)]
18. Chen, Q.; Jin, J.; Kou, Z.; Liao, C.; Liu, Z.; Zhou, L.; Wang, J.; Mai, L.J.S.  $Zn^{2+}$  pre-intercalation stabilizes the tunnel structure of  $MnO_2$  nanowires and enables zinc-ion hybrid supercapacitor of battery-level energy density. *Small* **2020**, *16*, 2000091. [[CrossRef](#)]
19. Duan, H.; Song, Z.; Miao, L.; Li, L.; Zhu, D.; Gan, L.; Liu, M. Unraveling the role of solvent–precursor interaction in fabricating heteroatomic carbon cathode for high-energy-density Zn-ion storage. *J. Mater. Chem. A* **2022**, *10*, 9837–9847. [[CrossRef](#)]
20. Liu, L.; Wu, Y.-C.; Huang, L.; Liu, K.; Duployer, B.; Rozier, P.; Taberna, P.-L.; Simon, P. Alkali ions pre-intercalated layered  $MnO_2$  nanosheet for zinc-ions storage. *Adv. Energy Mater.* **2021**, *11*, 2101287. [[CrossRef](#)]
21. Yuan, Y.; Zhan, C.; He, K.; Chen, H.; Yao, W.; Sharifi-Asl, S.; Song, B.; Yang, Z.; Nie, A.; Luo, X.; et al. The influence of large cations on the electrochemical properties of tunnel-structured metal oxides. *Nat. Commun.* **2016**, *7*, 13374. [[CrossRef](#)]
22. Zhao, R.; Zhang, L.; Wang, C.; Yin, L. Tetramethyl ammonium cation intercalated layered birnessite manganese dioxide for high-performance intercalation pseudocapacitor. *J. Power Sources* **2017**, *353*, 77–84. [[CrossRef](#)]
23. Wang, X.; Hu, P.; Niu, C.; Meng, J.; Xu, X.; Wei, X.; Tang, C.; Luo, W.; Zhou, L.; An, Q.; et al. New-type  $K_{0.7}Fe_{0.5}Mn_{0.5}O_2$  cathode with an expanded and stabilized interlayer structure for high-capacity sodium-ion batteries. *Nano Energy* **2017**, *35*, 71–78. [[CrossRef](#)]
24. Kang, K.; Ceder, G. Factors that affect Li mobility in layered lithium transition metal oxides. *Phys. Rev. B* **2006**, *74*, 094105. [[CrossRef](#)]
25. Nam, K.W.; Kim, S.; Yang, E.; Jung, Y.; Levi, E.; Aurbach, D.; Choi, J.W. Critical role of crystal water for a layered cathode material in sodium ion batteries. *Chem. Mater.* **2015**, *27*, 3721–3725. [[CrossRef](#)]
26. Frey, N.C.; Byles, B.W.; Kumar, H.; Er, D.; Pomerantseva, E.; Shenoy, V.B. Prediction of optimal structural water concentration for maximized performance in tunnel manganese oxide electrodes. *Phys. Chem. Chem. Phys.* **2018**, *20*, 9480–9487. [[CrossRef](#)] [[PubMed](#)]
27. Zhang, J.; Sun, J.; Ahmed Shifa, T.; Wang, D.; Wu, X.; Cui, Y. Hierarchical  $MnO_2$ /activated carbon cloth electrode prepared by synchronized electrochemical activation and oxidation for flexible asymmetric supercapacitors. *Chem. Eng. J.* **2019**, *372*, 1047–1055. [[CrossRef](#)]
28. Xu, Z.; Sun, S.; Cui, W.; Lv, J.; Geng, Y.; Li, H.; Deng, J. Interconnected network of ultrafine  $MnO_2$  nanowires on carbon cloth with weed-like morphology for high-performance supercapacitor electrodes. *Electrochim. Acta* **2018**, *268*, 340–346. [[CrossRef](#)]
29. Guo, C.; Liu, H.; Li, J.; Hou, Z.; Liang, J.; Zhou, J.; Zhu, Y.; Qian, Y. Ultrathin  $\delta-MnO_2$  nanosheets as cathode for aqueous rechargeable zinc ion battery. *Electrochim. Acta* **2019**, *304*, 370–377. [[CrossRef](#)]
30. Chen, J.; Wang, X.; Wang, J.; Lee, P.S. Sulfidation of NiMn-layered double hydroxides/graphene oxide composites toward supercapacitor electrodes with enhanced performance. *Adv. Energy Mater.* **2016**, *6*, 1501745. [[CrossRef](#)]
31. Lan, B.; Huang, S.; Ye, C.; Qin, Q.; Yan, J.; Wu, Y. Enhanced electrochemical performance of Sn-doped  $MnO_2$  and study on morphology evolution. *J. Alloys Compd.* **2019**, *788*, 302–310. [[CrossRef](#)]
32. Long, X.; Tian, L.; Wang, J.; Zhang, L.; Chen, Y.; Emin, A.; Wang, X.; Xie, W.; Liu, D.; Fu, Y.; et al. Interconnected  $\delta-MnO_2$  nanosheets anchored on activated carbon cloth as flexible electrode for high-performance aqueous asymmetric supercapacitors. *J. Electroanal. Chem.* **2020**, *877*, 114656. [[CrossRef](#)]
33. Nasser, R.; Zhang, G.-F.; Song, J.-M. Facile and low-cost synthesis of cobalt-doped  $MnO_2$  decorated with graphene oxide for high performance 2.3 V aqueous asymmetric supercapacitors. *Electrochim. Acta* **2020**, *345*, 136198. [[CrossRef](#)]
34. Gu, Y.-J.; Wen, W.; Wu, J.-M. Wide potential window  $TiO_2$ @carbon cloth and high capacitance  $MnO_2$ @carbon cloth for the construction of a 2.6 V high-performance aqueous asymmetric supercapacitor. *J. Power Sources* **2020**, *469*, 228425. [[CrossRef](#)]
35. Zong, Q.; Zhang, Q.; Mei, X.; Li, Q.; Zhou, Z.; Li, D.; Chen, M.; Shi, F.; Sun, J.; Yao, Y.; et al. Facile synthesis of na-doped  $MnO_2$  nanosheets on carbon nanotube fibers for ultrahigh-energy-density all-solid-state wearable asymmetric supercapacitors. *ACS Appl. Mater. Interfaces* **2018**, *10*, 37233–37241. [[CrossRef](#)] [[PubMed](#)]
36. Sehrawat, D.; Rawal, A.; Cheong, S.; Avdeev, M.; Ling, C.D.; Kimpton, J.A.; Sharma, N. Alkali metal-modified  $P2 Na_xMnO_2$ : Crystal structure and application in sodium-ion batteries. *Inorg. Chem.* **2020**, *59*, 12143–12155. [[CrossRef](#)]
37. Chen, S.; Zhang, M.; Ma, X.; Li, L.; Zhou, X.; Zhang, Z. Asymmetric supercapacitors by integrating high content  $Na^+/K^+$ -inserted  $MnO_2$  nanosheets and layered  $Ti_3C_2X$  paper. *Electrochim. Acta* **2020**, *332*, 135497. [[CrossRef](#)]
38. Kulkarni, S.; Puthusseri, D.; Thakur, S.; Banpurkar, A.; Patil, S. Hausmannite manganese oxide cathodes for supercapacitors: Surface wettability and electrochemical properties. *Electrochim. Acta* **2017**, *231*, 460–467. [[CrossRef](#)]
39. Singu, B.S.; Yoon, K.R. Exfoliated graphene-manganese oxide nanocomposite electrode materials for supercapacitor. *J. Alloys Compd.* **2019**, *770*, 1189–1199. [[CrossRef](#)]
40. Pendashteh, A.; Senokos, E.; Palma, J.; Anderson, M.; Vilatela, J.J.; Marcilla, R. Manganese dioxide decoration of macroscopic carbon nanotube fibers: From high-performance liquid-based to all-solid-state supercapacitors. *J. Power Sources* **2017**, *372*, 64–73. [[CrossRef](#)]
41. Shao, J.; Zhou, X.; Liu, Q.; Zou, R.; Li, W.; Yang, J.; Hu, J. Mechanism analysis of the capacitance contributions and ultralong cycling-stability of the isomorphous  $MnO_2@MnO_2$  core/shell nanostructures for supercapacitors. *J. Mater. Chem. A* **2015**, *3*, 6168–6176. [[CrossRef](#)]
42. Jabeen, N.; Xia, Q.; Saviolov, S.V.; Aldoshin, S.M.; Yu, Y.; Xia, H. Enhanced pseudocapacitive performance of  $\alpha-MnO_2$  by cation preinsertion. *ACS Appl. Mater. Interfaces* **2016**, *8*, 33732–33740. [[CrossRef](#)] [[PubMed](#)]

43. Wu, P.; Gao, M.; Yu, S.; Feng, M.; Liu, S.; Fu, J. MnO<sub>2</sub> nanosheets grown on N and P co-doped hollow carbon microspheres for high performance asymmetric supercapacitor. *Electrochim. Acta* **2020**, *354*, 136681. [[CrossRef](#)]
44. Li, Y.; Xu, Z.; Wang, D.; Zhao, J.; Zhang, H. Snowflake-like core-shell  $\alpha$ -MnO<sub>2</sub>@ $\delta$ -MnO<sub>2</sub> for high performance asymmetric supercapacitor. *Electrochim. Acta* **2017**, *251*, 344–354. [[CrossRef](#)]
45. Peng, H.; Fan, H.; Sui, J.; Wang, C.; Zhang, W.; Wang, W. Sodium in situ intercalated ultrathin  $\delta$ -MnO<sub>2</sub> flakes electrode with enhanced intercalation capacitive performance for asymmetric supercapacitors. *ChemistrySelect* **2020**, *5*, 869–874. [[CrossRef](#)]
46. Jiang, L.; Dong, M.; Dou, Y.; Chen, S.; Liu, P.; Yin, H.; Zhao, H. Manganese oxides transformed from orthorhombic phase to birnessite with enhanced electrochemical performance as supercapacitor electrodes. *J. Mater. Chem. A* **2020**, *8*, 3746–3753. [[CrossRef](#)]
47. Patil, S.J.; Chodankar, N.R.; Han, Y.-K.; Lee, D.W. Carbon alternative pseudocapacitive V<sub>2</sub>O<sub>5</sub> nanobricks and  $\delta$ -MnO<sub>2</sub> nanoflakes @  $\alpha$ -MnO<sub>2</sub> nanowires hetero-phase for high-energy pseudocapacitor. *J. Power Sources* **2020**, *453*, 227766. [[CrossRef](#)]
48. Chen, Y.; Jing, C.; Fu, X.; Shen, M.; Cao, T.; Huo, W.; Liu, X.; Yao, H.-C.; Zhang, Y.; Yao, K.X. In-situ fabricating MnO<sub>2</sub> and its derived FeOOH nanostructures on mesoporous carbon towards high-performance asymmetric supercapacitor. *Appl. Surf. Sci.* **2020**, *503*, 144123. [[CrossRef](#)]
49. Yuan, X.; Zhang, Y.; Yan, Y.; Wei, B.; Qiao, K.; Zhu, B.; Cai, X.; Chou, T.-W. Tunable synthesis of biomass-based hierarchical porous carbon scaffold@MnO<sub>2</sub> nanohybrids for asymmetric supercapacitor. *Chem. Eng. J.* **2020**, *393*, 121214. [[CrossRef](#)]
50. Tangarnjanavalukul, C.; Phattharasapakun, N.; Kongpatpanich, K.; Sawangphruk, M. Charge storage performances and mechanisms of MnO<sub>2</sub> nanospheres, nanorods, nanotubes and nanosheets. *Nanoscale* **2017**, *9*, 13630–13639. [[CrossRef](#)] [[PubMed](#)]
51. Nagaraju, G.; Ko, Y.H.; Cha, S.M.; Im, S.H.; Yu, J.S. A facile one-step approach to hierarchically assembled core-shell-like MnO<sub>2</sub>@MnO<sub>2</sub> nanoarchitectures on carbon fibers: An efficient and flexible electrode material to enhance energy storage. *Nano Res.* **2016**, *9*, 1507–1522. [[CrossRef](#)]
52. Guo, Y.; Li, L.; Song, L.; Wu, M.; Gao, Y.; Chen, J.; Mao, C.; Song, J.; Niu, H. Co<sup>2+</sup> induced phase transformation from  $\delta$ - to  $\alpha$ -MnO<sub>2</sub> and their hierarchical  $\alpha$ -MnO<sub>2</sub>@ $\delta$ -MnO<sub>2</sub> nanostructures for efficient asymmetric supercapacitors. *J. Mater. Chem. A* **2019**, *7*, 12661–12668. [[CrossRef](#)]
53. Rogier, C.; Pognon, G.; Bondavalli, P.; Galindo, C.; Nguyen, G.T.M.; Vancaeyzeele, C.; Aubert, P.-H. Electrodeposition of MnO<sub>2</sub> on spray-coated nanostructured carbon framework as high performance material for energy storage. *Surf. Coat. Technol.* **2020**, *384*, 125310. [[CrossRef](#)]
54. Peng, H.; Fan, H.; Yang, C.; Tian, Y.; Wang, C.; Sui, J. Ultrathin  $\delta$ -MnO<sub>2</sub> nanoflakes with Na<sup>+</sup> intercalation as a high-capacity cathode for aqueous zinc-ion batteries. *RSC Adv.* **2020**, *10*, 17702–17712. [[CrossRef](#)] [[PubMed](#)]
55. Yang, Y.; Niu, H.; Qin, F.; Guo, Z.; Wang, J.; Ni, G.; Zuo, P.; Qu, S.; Shen, W. MnO<sub>2</sub> doped carbon nanosheets prepared from coal tar pitch for advanced asymmetric supercapacitor. *Electrochim. Acta* **2020**, *354*, 136667. [[CrossRef](#)]
56. Zhang, M.; Zheng, H.; Zhu, H.; Xu, Z.; Liu, R.; Chen, J.; Song, Q.; Song, X.; Wu, J.; Zhang, C.; et al. Graphene-wrapped MnO<sub>2</sub> achieved by ultrasonic-assisted synthesis applicable for hybrid high-energy supercapacitors. *Vacuum* **2020**, *176*, 109315. [[CrossRef](#)]
57. Feng, W.; Liu, G.; Wang, P.; Zhou, J.; Gu, L.; Chen, L.; Li, X.; Dan, Y.; Cheng, X. Template synthesis of a heterostructured MnO<sub>2</sub>@SnO<sub>2</sub> hollow sphere composite for high asymmetric supercapacitor performance. *ACS Appl. Energy Mater.* **2020**, *3*, 7284–7293. [[CrossRef](#)]
58. Li, D.; Lin, J.; Lu, Y.; Huang, Y.; He, X.; Yu, C.; Zhang, J.; Tang, C. MnO<sub>2</sub> nanosheets grown on N-doped agaric-derived three-dimensional porous carbon for asymmetric supercapacitors. *J. Alloys Compd.* **2020**, *815*, 152344. [[CrossRef](#)]
59. Li, B.; Zhang, X.; Dou, J.; Zhang, P. Construction of MnO<sub>2</sub>@NH<sub>4</sub>MnF<sub>3</sub> core-shell nanorods for asymmetric supercapacitor. *Electrochim. Acta* **2020**, *347*, 136257. [[CrossRef](#)]
60. Tan, Y.; Yang, C.; Qian, W.; Teng, C. Flower-like MnO<sub>2</sub> on layered carbon derived from sisal hemp for asymmetric supercapacitor with enhanced energy density. *J. Alloys Compd.* **2020**, *826*, 154133. [[CrossRef](#)]
61. Zarshad, N.; Wu, J.; Rahman, A.U.; Ni, H. Fe-MnO<sub>2</sub> core-shell heterostructure for high-performance aqueous asymmetrical supercapacitor. *J. Electroanal. Chem.* **2020**, *871*, 114266. [[CrossRef](#)]
62. Fu, Y.; Gao, X.; Zha, D.; Zhu, J.; Ouyang, X.; Wang, X. Yolk-shell-structured MnO<sub>2</sub> microspheres with oxygen vacancies for high-performance supercapacitors. *J. Mater. Chem. A* **2018**, *6*, 1601–1611. [[CrossRef](#)]
63. Dudarev, S.L.; Botton, G.A.; Savrasov, S.Y.; Humphreys, C.J.; Sutton, A.P. Electron-energy-loss spectra and the structural stability of nickel oxide: An LSDA+ U study. *Phys. Rev. B* **1998**, *57*, 1505. [[CrossRef](#)]
64. Kitchaev, D.A.; Peng, H.; Liu, Y.; Sun, J.; Perdew, J.P.; Ceder, G. Energetics of MnO<sub>2</sub> polymorphs in density functional theory. *Phys. Rev. B* **2016**, *93*, 045132. [[CrossRef](#)]
65. Franchini, C.; Podloucky, R.; Paier, J.; Marsman, M.; Kresse, G. Ground-state properties of multivalent manganese oxides: Density functional and hybrid density functional calculations. *Phys. Rev. B* **2007**, *75*, 195128. [[CrossRef](#)]